Validity of Crystal Plasticity Models Near Grain Boundaries: Contribution of Elastic Strain Measurements at Micron Scale

EMERIC PLANCHER,[1] POUYA TAJDARY,[1] THIERRY AUGER,[1,5] OLIVIER CASTELNAU,[1] VÉRONIQUE FAVIER,[1] DOMINIQUE LOISNARD,[2] JEAN-BAPTISTE MARIJON,[1] CLAIRE MAURICE,[4] VINCENT MICHEL,[1] ODILE ROBACH,[3] and JULIEN STODOLNA[2]

1.—PIMM, UMR 8006, CNRS-Ensam-CNAM, 151 Bld de l'hôpital, 75013 Paris, France 2.—Département MMC, EDF, Avenue des renardières, 77818 Moret-sur-Loing, France 3.—CEA–CNRS CRG-IF BM32 beamline at ESRF, 6 rue Jules Horowitz, Cedex 9, 38043 Grenoble, France. 4.—Laboratoire Georges Friedel, UMR CNRS 5307, Mines Saint-Etienne, 158 cours Fauriel, 42100 Saint-Étienne, France. 5.—e-mail: thierry.auger@ensam.eu

Synchrotron Laue microdiffraction and digital image correlation measurements were coupled to track the elastic strain field (or stress field) and the total strain field near a general grain boundary in a bent bicrystal. A 316L stainless steel bicrystal was deformed in situ into the elasto-plastic regime using a four-point bending setup. The test was then simulated using finite elements with a crystal plasticity model comprising internal variables (dislocation densities on discrete slip systems). The predictions of the model are compared with both the total strain field and the elastic strain field obtained experimentally. While activated slip systems and total strains are reasonably well predicted, elastic strains appear overestimated next to the grain boundary. This suggests that conventional crystal plasticity models need improvement to correctly model stresses at grain boundaries.

INTRODUCTION

The buildup of intergranular microstresses (type II internal stresses) and intragranular stresses or residual stresses (type III internal stresses) upon plastic deformation is a central issue in mechanics of materials.[1] The development of local stresses is generally due to incompatibilities between the anisotropic (elastic and plastic) deformation on both sides of grain boundaries. Another contribution to internal stresses is associated with spatial localization patterns at the microstructural scale of plastic deformation. Since plasticity precedes many other metallurgical phenomena such as recrystallization, phase transformations, or damage, its correct understanding (i.e., the ability to reliably predict local stress/strain fields in a plastically deformed material) has major implications; For example, the simulation of intergranular stresses is critical to describe environmental effects such as stress corrosion cracking or liquid metal embrittlement, because intergranular stresses drive the dynamics of fracture.[2–4] During recrystallization, the stored elastic energy associated with the dislocation network governs the microstructure evolution.[5,6] It is therefore desirable to quantify the degree of accuracy of local stress/strain fields that one can achieve through simulation, by comparing experimentally accessible stress and strain fields with modeling results in polycrystals.

Measurement of internal stresses is usually performed by x-ray or neutron diffraction analysis, using a beam cross-section significantly larger than the grain size. Those techniques often lead to a reasonably accurate but averaged estimation of microstrains[7] that compares well with plastic texture simulations.[8–10] Recently, the advent of local probes such as digital image correlation (DIC),[11] high-angular-resolution electron backscatter diffraction (HR-EBSD),[12,13] and synchrotron Laue microdiffraction[14,15] has opened the way to a new class of measurements that can directly map mechanical fields to a high degree of accuracy, down to micrometer spatial resolution. Therefore,

full-field measurements can be carried out at the same scale as microstructural models featuring crystal plasticity constitutive laws, paving the way to advanced validation of scale-transition modeling.

One of the key questions raised when using crystal plasticity models is whether grain boundaries can be treated as sole geometrical interphases, as thin surfaces with specific properties and special kinematics conditions,[16] or as nonlocal microstructural constituents with special properties per se.[17] Grain boundaries are obstacles to dislocation slip, but depending upon their nature or the misorientation between adjacent grains, they may still transmit some amount of plastic deformation from one grain to the other.[18] Conventional crystal plasticity models, such as that employed herein,[19,20] do not define any particular behavior for the grain boundary, an assumption that may not be realistic enough.

In this work, a concentrated austenitic solid solution, typical of 316L stainless steel, is employed as a model alloy. We report herein an original comparison between two mechanical fields measured at similar and fine spatial resolution, viz. elastic and total (elastic + plastic) strain fields versus the prediction of a local crystal plasticity simulation.[19] First, the crystal plasticity parameters were fit for the alloy and the set of parameters validated by considering experimental fields developing in a single crystal.[21,22] Then, an in situ bending experiment was performed at the European ESRF synchrotron to investigate how both strain fields localize near a general grain boundary in a large bicrystal. Strain measurements were performed near the grain boundary at several loading steps using optical DIC (total strains) and Laue microdiffraction (elastic strains). The agreement between the prediction of the finite element simulation and the experimental data is discussed for both strain fields and the local activation of slip systems.

EXPERIMENTAL PROCEDURES

Materials

Macroscopic single crystals of high-purity austenitic stainless steel were grown by Bridgman directional solidification in a horizontal furnace with argon cover gas. For tensile and bending experiments, single-crystal samples were cut by spark erosion from a macroscopic single crystal, with the crystal axes aligned with the sample axes within 3°. A bicrystal bending sample was also cut out from a macroscopic oligocrystal obtained in a separate crystal growth attempt. The grain boundary was selected for its position, considering the geometrical requirements for the bending sample, thus its character was random. Therefore, the chemical compositions of the bicrystal and the single crystals differ slightly (Table I). The gauge section of the two tensile specimens had dimensions of 8 mm × 3 mm × 0.5 mm. The dimensions of the single-crystal bending specimen were 30 mm × 4.3 mm × 0.46 mm. The dimensions of the bicrystal bending specimen were 30 mm × 4.8 mm × 0.48 mm. All samples were carefully polished to 1 μm grade or below, and the preparation quality checked using channeling contrast imaging in a scanning electron microscope. Details of the single-crystal bending and tensile experiments are reported in Ref. 22. The elastic constants of the 316L oligocrystal were measured by resonant ultrasound spectroscopy, yielding values of C_{11} = 202 GPa, C_{12} = 130 GPa, and C_{44} = 128 GPa (with estimated uncertainty below ± 1 GPa).

Laue Microdiffraction and DIC Under Synchrotron Radiation

In situ Laue microdiffraction experiments were carried out at the French CRG beamline BM32 of the European Synchrotron (ESRF, Grenoble, France), described in Ref. 23. The incoming polychromatic x-ray beam (energy range 5 keV to 23 keV) was focused down to ~ 800 nm × 600 nm by means of Kirkpatrick–Baez mirrors. Laue patterns were recorded using a MARCCD® detector (pixel size 79.14 μm, 2048 × 2048 pixels, 16 bits dynamic) positioned 60 mm above the specimen surface. A strain-free Ge wafer was used to calibrate the setup geometry (detector orientation, etc.). A custom-designed four-point bending rig was installed on the translation stage pretilted at 40°. The device was equipped with a load cell with capacity of 20 N and an extensometer sensitive to displacements below 1 μm to measure the macroscopic force/displacement imposed on the sample.

An optical microscope available on beamline BM32 (Allied Vision Technology GiGE®, Objective Mitutoyo 10 ×/0.28, f = 200) was employed in situ to acquire optical images for the measurement of the

Table I. Chemical composition of the high-purity alloys (single crystal and bicrystal)

Wt.%	Fe	Cr	Ni	Mo	C	Mn, N, S, P, Si, Cu, O
Monocrystal tensile	Bal.	17	14.6	2.3	< 0.002	Not detected
Monocrystal four-point bending	Bal.	17	14.6	2.3	< 0.002	Not detected
Bicrystal four-point bending	Bal.	15.5	14	1.7	< 0.002	Not detected

total strain field on the specimen cross-section surface by the DIC technique. MoS_2 powder (MOLYKOTE® Microsize, submicron grain size) was deposited on the sample surface to create a random speckle pattern. When a DIC image is to be acquired, the optical microscope must be positioned such that its focal plane covers the sample cross-section surface. Therefore, measurements were carried out sequentially, with the microscope being brought in and out between loading steps. Further details of the experimental setup can be found in Ref. 22.

Processing of the Laue microdiffraction data was performed using LaueTools software (see, e.g., Ref. 24) to extract the deviatoric part of the elastic deformation tensor.[25] In this work, the full elastic strain tensor was recovered assuming a vanishing stress vector on the specimen surface, which is a valid approximation due to the small attenuation length of x-rays (65 microns in Fe at 22 keV) and the lack of in-depth microstructure gradients in the specimen. The plane-stress hypothesis was used to determine the hydrostatic part of the stress tensor, then, using generalized Hook's law, the hydrostatic part of the elastic strain tensor was extracted. Laue patterns consisted mostly of a single diffraction figure, except on the grain boundary, where two overlapping figures could be detected. In that case, the figure with the more intense diffraction peak was indexed and associated with the relevant grain. The area investigated on the sample was approximately 400 μm × 600 μm, centered on the grain boundary with step size of 25 μm. Orientation angles use the Bunge convention in degrees throughout the paper $\varphi_1, \Phi, \varphi_2$). The maximum measured lattice rotation between the initial state and the loaded state reaches 2.5° point to point (in the scanned area).

MODELING

Formulation

The kinematics of the crystal plasticity model relies on the finite transformation framework (small elastic distortions but large lattice rotations) first proposed by Lee, where the deformation gradient tensor is constructed as the product of an elastic part with a plastic part.[26] The elastic part embodies the anisotropic elastic stretch and the grain rotation, while the plastic part accounts for crystallographic slipping along specific slip systems (up to 12 for a face-centered cubic crystal). The constitutive laws rely on dislocation densities resolved on each slip system as internal variables ρ^s whose evolution models strain hardening in metals and alloys. At each time increment of the computation, the local critical shear stress τ_c^s is computed with the updated dislocation densities using the forest hardening interaction matrix resolved on every slip system, via the a^{su} interaction matrix between slip systems (s and u) including diagonal self-interaction terms:[27]

$$\tau_c^s = \tau_0 + \mu b \sqrt{\sum_{u=1,12} a^{su} \rho^u}, \tag{1}$$

where μ is the isotropic shear modulus, b is the norm of the Burgers vector, and τ_0 is the lattice friction stress. The onset of slip is triggered according to the Schmid law. The rate-dependent slip rate prescription proposed by Pierce[28] for single crystals is used, approximated using a power law:

$$\dot{\gamma}^s = \dot{\gamma}_0 \left(\frac{|\tau^s|}{\tau_c^s} \right)^n \text{sign}(\tau^s) \quad \text{if} |\tau^s| > \tau_c^s, \dot{\gamma}^s = 0 \quad \text{otherwise}, \tag{2}$$

where $\dot{\gamma}_0$ is a reference shear rate and n is the stress sensitivity parameter. These material parameters are to be fit to reproduce the correct flow stress rate dependence. Following Teodosiu's law with the hypothesis of a constant mobile dislocation density,[19] the rate of evolution of the stored dislocation density is governed by a dislocation production term and is balanced by a dislocation annihilation term taking into account the dynamic recovery during deformation (related to the annihilation distance of dislocation dipoles y_c):

$$\dot{\rho}^s = \frac{|\dot{\gamma}^s|}{b} \left[\frac{\sqrt{\sum_{u \neq s} \rho^u}}{K} - 2 y_c \rho^s \right], \tag{3}$$

where K and y_c are material parameters that are usually fit to reproduce stage I and stage II on a single crystal. The approach is implemented in the Abaqus® finite element code, using a UMAT subroutine.[29]

Parameter Identification

Crystal plasticity parameters for 316L stainless steels can be found in several works.[4,30] There are three categories of parameters. The first comprises physical parameters that can be set based on the metallurgical state of the sample (Burgers vector, initial dislocation density ρ_0, and initial critical friction stress τ_0). (As stated above, the 316L elastic constants are taken as C_{11} = 202 GPa, C_{12} = 130 GPa, and C_{44} = 128 GPa.) The second set of parameters allows the description of viscous or rate-dependent effects ($\dot{\gamma}_0$ and n). For 316L stainless steel, it is important to set these parameters carefully, because austenitic steels are known to have a nonvanishing rate-dependent flow stress that becomes negligible only below strain rate of 10^{-2} s^{-1}.[31] For our purpose of testing at slow strain rate (i.e., lower than 10^{-2} s^{-1}), these parameters were constrained to correctly reproduce a quasistatic loading state with a minimized strain rate effect ($\dot{\gamma}_0 > 10^{-5}$ s^{-1} and $n > 20$). In order to perform this identification, tensile tests carried out on single

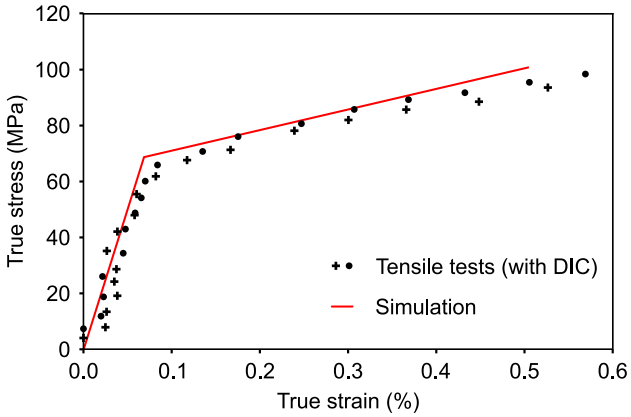

Fig. 1. Elasto-plastic response of a single crystal deformed under uniaxial tension along [100] direction. Experimental data are compared with the identified constitutive relation.

crystals at a strain rate of 10^{-4} s^{-1} along direction [100], as detailed in Ref. 22, were modeled by finite elements in Abaqus using C3D8 elements with [100] crystal orientation. The parameters τ_0, $\dot{\gamma}_0$, and n were then adjusted to fit the experimental curves (Fig. 1). The smooth transition at the onset of plasticity given by the Pierce strain rate law is damped due to our choice of parameters.

The third category of parameters (describing strain hardening) is composed first of the a^{su} interaction matrix between the slip systems and the two material parameters K and y_c. The interaction matrix (a_0 for self-interaction, a_1 for collinear interactions, a_2 for Lomer–Cottrell locks, a_3 for Hirth junctions, a_4 for glissile dislocation interactions, $a_5 = a_0$ for sessile dislocation interactions) is taken from the work of Devincre et al.[32], which was later applied for 316L(N) stainless steel.[30] The two remaining parameters were set to reproduce the slope of the single-crystal tensile curves reported in Fig. 1. It is known, however, that K and y_c may vary with the strain level, and our choice may need to be refit to better reproduce a larger amount of experimental data.

Overall, the resulting parameters are presented in Table II along with, when applicable, their values as found in two other works in which a rate-dependent crystal plasticity approach was used.[4,30] The major differences between different parametrizations can be rationalized by being due either to a compositional difference with our alloys or to a different initial dislocation density (ρ_0 and τ_0 act in synergy to give a larger flow stress than our well-annealed alloys).

This parametrization was validated against the measurement of the elastic strain and total strain fields, performed by Laue microdiffraction and DIC, respectively, along the specimen cross-section, in the bending experiment of a 316L single crystal (see Ref. 22). For the simulation, the dimensions of the sample were 0.46 mm × 4.3 mm × 30 mm, and the [100] orientation was aligned with the loading axis. The four-point bending test configuration was simulated by adding four rigid cylindrical shells (outer shells fixed; inner shells moving along Ox axis). The contact interaction conditions between the four pins and the single-crystal beam were frictionless sliding. The boundary condition displacement rate imposed for the simulation was set to be in the quasistatic strain rate domain of the crystal plasticity model. The beam deflection was simulated up to the final measured one. Figure 2 shows that the total strain and elastic strain profiles were reproduced rather accurately along the cross-section of the sample. The stress–strain curve of the single crystal oriented for multiple slips did not present stage I, but stage II. It reproduces nicely the transition from elastic to plastic deformation, together with the slope of elastic strain in the plastic regions associated with crystal hardening. This provides confidence that the crystal plasticity parameters are correctly set according to the fitting strategy described herein.

EXPERIMENTAL AND MODELING SETUP FOR THE BICRYSTAL

A schematic view of the investigated bicrystal is shown in Fig. 3. The supposedly planar grain boundary was inclined with respect to the specimen axes as indicated. The misorientation angle between the two grains is 64°, specifying a general grain boundary. The specimen was loaded in situ in the four-point loading device using the setup described in "Laue Microdiffraction and DIC Under Synchrotron Radiation" section. Sample deformation was carried out step by step, and measurements were performed at 0 N (initial state), 3 N, and 7 N, then after complete unloading. After each load increment, the pin displacement was blocked, and we waited until the specimen relaxation was complete (∼ 20 min). Then, a Laue map covering the area of the grain boundary was obtained. DIC mapping measurements were also carried out at each Laue step while keeping the sample under load. The lower and upper grains are labeled grain 1 and grain 2, respectively.

The modeling of crystal plasticity in the bicrystal bend test was performed similarly to the single crystal by simulating the entire bicrystal in Abaqus (dimensions 0.48 mm × 4.8 mm × 30 mm). The beam was split into two parts with a slanted surface representing the grain boundary (at an angle of 50° in the x–y plane and 37° in the y–z plane). The mesh for the finite element modeling was then generated using C3D8 elements with a fine grid close to the grain boundary and a coarser grid further away to save computational power. The fine–coarse separation was set manually to model with a coarse mesh the part of the beam that stays in the elastic regime so that the entire plastically deformed volume was covered with a fine mesh. The four-point bending

Table II. Crystal plasticity physical parameters used for the 316L stainless steel

	b (m)	ρ_0 (m^{-2})	τ_0 (MPa)	$\dot{\gamma}_0$ (s^{-1})	n	K	y_c (m)	a_0	a_1	a_2	a_3
This work	2.54×10^{-10}	1.6×10^{10}	22.3	10^{-4}	40	18	1.25×10^{-9}	0.1388	0.633	0.079	0.1236
[30]	2.54×10^{-10}	1.72×10^{12}	22.3	4×10^{-11}	73.5	59.97	1.29×10^{-9}	0.1388	0.633	0.079	0.1236
[4]		N.R.	90	10^{-3}	55	N.A.	N.A.	N.A.	N.A.	N.A.[a]	N.A.[a]

When a unit is not specified, the parameter is nondimensional*N.A.* not applicable, *N.R.* not reported[a]Note that there is an inversion between a_2 and a_3 in Ref. 30 compared with Ref. 32.

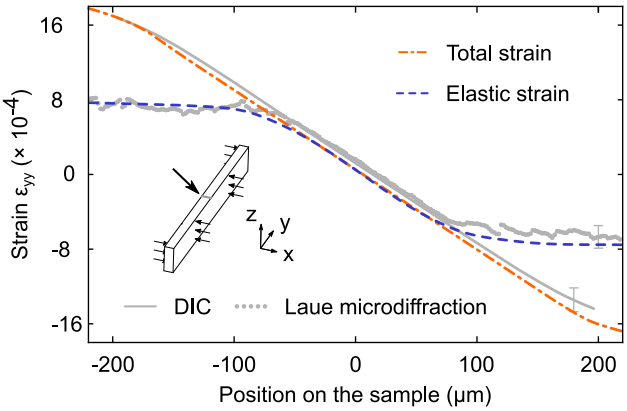

Fig. 2. Elastic and total (i.e., elastic + plastic) strain evolution across the thickness of a [100] bent single crystal. The positions of measurement points are along *x* direction on the surface normal to *z* (inset). Experimental data from DIC and Laue microdiffraction (grey curves) are compared with the identified crystal plasticity model (blue and red curves) (Color figure online).

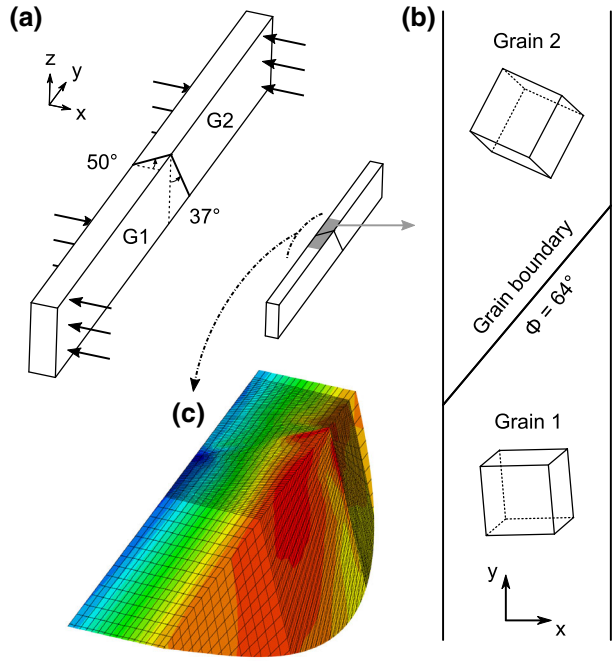

Fig. 3. Geometry of the in-situ setup: (a) Schematic of four-point bending experiment performed on a 316L bicrystal (b) Euler angles for grains G1 and G2 are (−175°, 78°, −107°) and (−133°, 25°, −163°) respectively (c) details of the FEM mesh next to the grain boundary.

test configuration was simulated by adding four rigid cylindrical shells with identical boundary conditions and contact interactions. The displacement rate used for the simulation was small enough to be in the quasistatic loading state of the crystal plasticity model. The total strain was given as a result of the nonlinear finite element modeling, while the elastic strain was extracted at each step by elastically unloading the current stress using the generalized Hooke's law in the crystal reference frame. The elastic strain tensor was then rotated back to the sample reference frame to be readily compared with the measured one.

RESULTS ON THE BICRYSTAL

After complete unloading, the pattern formed by the MoS_2 deposit used for DIC at the surface of the bicrystal was cleaned in an ultrasonic bath. The sample surface was then observed using channeling contrast in a scanning electron microscope adapted for large field of view observations with low image distortions (TESCAN MIRA3®). The backscattered electron image shown in Fig. 4 reveals the grain boundary and multiple slip traces observed in both grains. In grain 2, slip trace analysis using the orientation data from Laue microdiffraction ($\varphi_1 = -133°$, $\Phi = 25°$, $\varphi_2 = -163°$) can provide the slip planes associated with the four families of traces observed. In grain 1 ($\varphi_1 = -175°$, $\Phi = 78°$, $\varphi_2 = -107°$) the slip traces associated with slip planes (− 111) and (111) are very close to a theoretical misorientation in the surface plane of only a few degrees.

To compare with the slip systems activated in the simulation, the area of interest was schematically sliced into 12 domains and the number of active systems tallied. The division was based on (1) approximate distance from the grain boundary and (2) the nature of the applied stress (tensile,

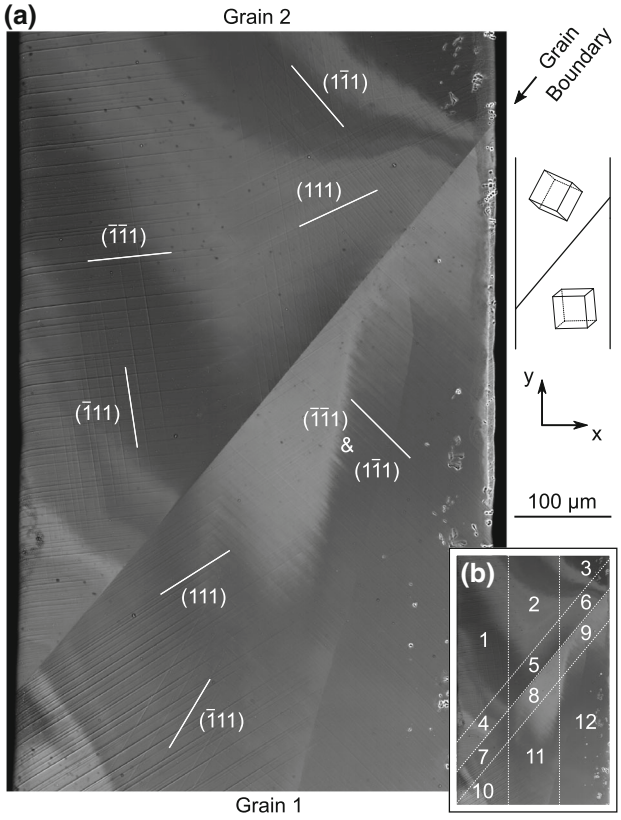

Fig. 4. Backscatter electron image of area of interest after complete unloading. (a) Slip trace patterns are detected in both grains, revealing single or multiple slip activation. Slip trace analysis was performed to identify the slip planes associated with the different families of slip traces. (b) Division of area into 12 regions used to compare with the finite element model.

compressive, or near-neutral fiber). The activated slip systems and corresponding dislocation density were extracted from the simulation as state variables. In the domains where a slip system was not activated ($|\tau^s| < \tau_c^s$ or $\dot{\gamma} < 10^{-6}\,\mathrm{s}^{-1}$ at all steps), the corresponding dislocation density variable remains constant. A visual one-to-one comparison between the slip traces in each domain from Fig. 4a and the activated slip systems given by a Schmid factor analysis was performed, revealing that the simulation correctly predicted the type and number of activated slip systems in all regions except 6 and 9 (which are closer to the grain boundary and are in the area which is subject to tensile stress). In the tensile part of the sample, according to the simulation, grain 1 should be in dual slip mode $(111)<01\bar{1}>$ and $(1\bar{1}1)<011>$, while grain 2 should be closer to single slip mode $(\bar{1}\bar{1}1)<101>$. However, in the experiment, due to internal stresses, not every predicted slip plane is activated. Grain 1 is rather deformed, and grain 2 tries to accommodate.

The experimental strain fields (total and elastic) were extracted following the procedure described above respectively from the DIC and Laue diffraction data. They are plotted for the *yy* component (along the *y* axis of Fig. 3) of the total strain tensor (Fig. 5) and of the elastic strain tensor (Fig. 6). The total strain ϵ^t_{yy} distribution shows that the right part of the specimen is mainly in tension while the left part is mainly in compression, as expected for bending. However, the grain boundary clearly disturbs the strain field. The strain magnitude is stronger in grain 1 than in grain 2. The simulation results for ϵ^t_{yy} are presented in Fig. 5b. One can see that the main plastic activity domains are very well reproduced, except at the top right corner. The normalized difference plot is shown in Fig. 5c. It reveals that the difference between the measurement and simulation results over almost the entire analyzed surface, including next to the grain boundary area, remains below 20%. This level of agreement is considered as being rather good.

The elastic strains ϵ^e_{yy} are shown in Fig. 6. One can see that the experimental elastic strains closely follow what is expected from a bending beam experiment. One clearly sees an area in tension at the right and an area in compression at the left, consistent with the existence of a neutral fiber in a four-point bending experiment. The effect of the grain boundary can be seen weakly, as some higher *yy* strain component appear as hot spots along the grain boundary. Figure 6b shows the simulated corresponding elastic strain. Overall, the shape looks similar, but the intensity scale is significantly different and appears globally to be of higher magnitude than that measured experimentally. The normalized difference plot is shown in Fig. 6c. The presence of a grain boundary can be easily inferred from this plot with two main sources of disagreement. The first is the presence of an area at the right of grain 1 (the area in tension) that seems to frequently show disagreement between the experimental data and simulation results. The other surprising characteristics is the clear distinction of the grain boundary as a major contributor to the disagreement between the experimental data and simulation results. This indicates that, next to the grain boundary, there is a special area where crystal plasticity somehow overestimates the elastic strains induced by the plastic activity due to bending. The elastic strain from a large part of grain 2 is well predicted, especially away from the grain boundary. This is expected as the area was only slightly plastically deformed (< 0.5%). The same conclusion can be reached for grain 1 close to the neutral fiber, but to a lesser extent.

DISCUSSION

In situ mapping of total and elastic strains by DIC and Laue microdiffraction allowed characterization of the evolution of these fields around a general grain boundary, with a model alloy of 316L, in a beam bending configuration. This constitutes a major step forward compared with similar studies aiming at measurement of elastic strains, such as

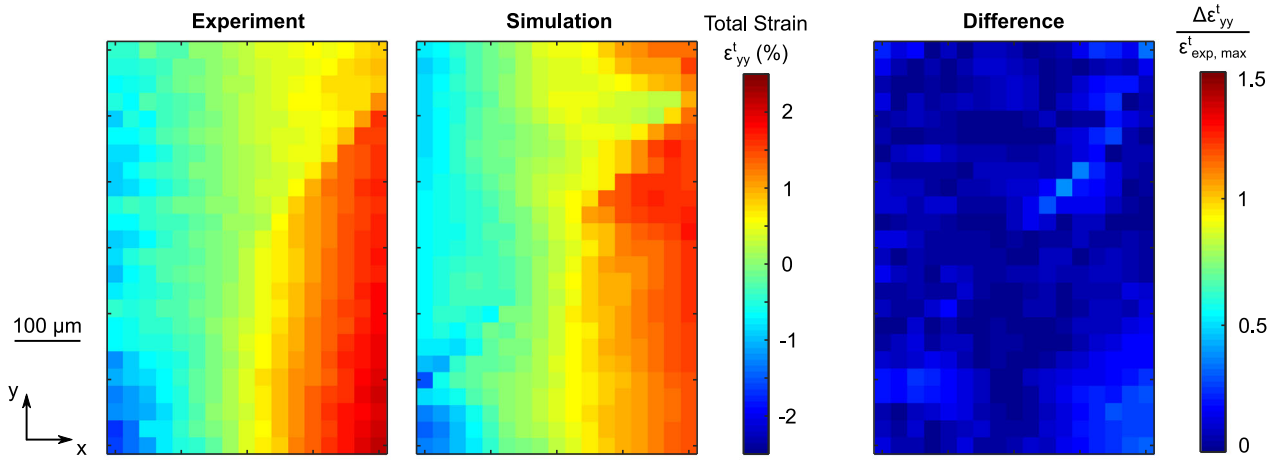

Fig. 5. Total strain fields along *y* axis: experimental, modeling, and difference plot at loading of 7 N.

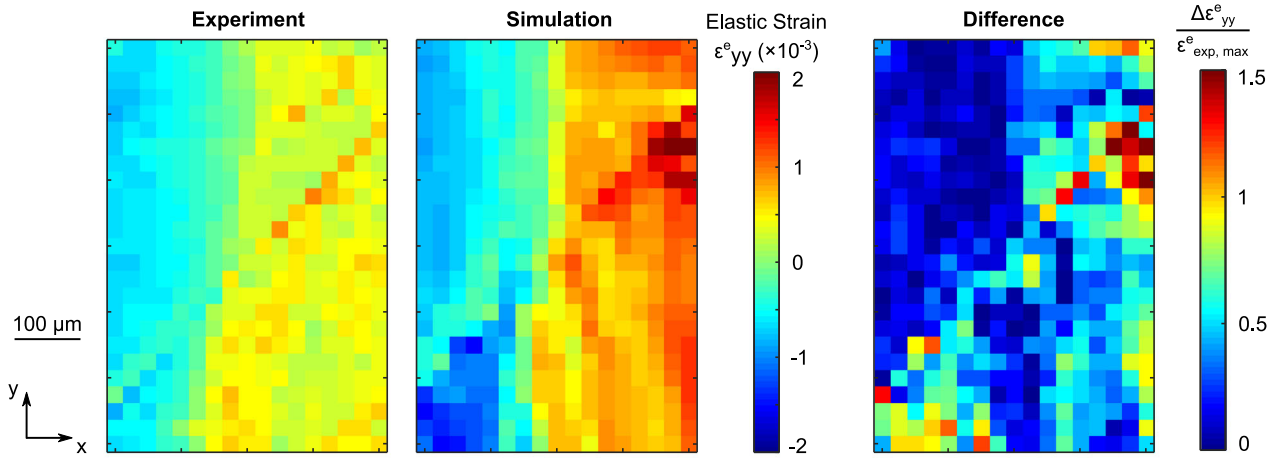

Fig. 6. Elastic strain fields along *y* axis: experimental, modeling, and difference plot at loading of 7 N.

those carried out a few years ago which had a beam size of 100 μm × 100 μm, compared with 1 μm × 1 μm here[33] or what can be achieved with high-energy x-ray diffraction analysis.[34] The currently achieved spatial resolution with Laue microdiffraction at synchrotron facilities allows this issue to be tackled with much higher accuracy.

The results of this work show that the heterogeneities in active slip planes are very well predicted with the formation of well-identified plastic domains in the different parts of the area surrounding the grain boundary. While some localized discrepancies arise at one edge of the specimen (more specifically at the right-hand side in the tensile area), one can note that the difference between the predicted domains and the observed ones is not specifically related to the grain boundary. The total strain field is also very well predicted. It is mainly controlled by the macroscopic kinematics, although the presence of grain boundary and the induced change in anisotropy clearly disturb the field around it. This work provides another example of the well-known effect of grain boundaries on the formation of plastic heterogeneities or plastic glide domains.[35,36] It also illustrates the ability of standard crystal plasticity modeling to predict in a detailed manner these early stages of plastic deformation (the maximum total strain here being less than 2%). The measured elastic strain field has mainly the symmetry induced by the bending geometry, but modified, to a lesser extent, by the presence of the grain boundary. Its prediction by conventional crystal plasticity is, on the other hand, much less accurate than for the total strain. Elastic strains and thus internal stresses are notably overestimated in the neighborhood of the grain boundary and in the right-hand corner of the analyzed area (grain 1). Away from the grain boundary, it is predicted correctly with accuracy better than 20% over more than 50% of the analyzed area.

Let us first discuss possible experimental artifacts. A possible source of discrepancy between the crystal plasticity model and experimental data

could come from the relaxation of the specimen. Here, elastic and total strains were measured when relaxation had terminated and the applied force stabilized. The typical stress drop between the end of the loading step and the relaxed state lies in the 5% to 20% range (see Ref. 22). Relaxation is associated with limited glide of a small number of dislocations to adjust and minimize internal stresses (microplastic regime). It therefore has a limited influence on the total strain field but affects the elastic one in a significant manner. Relaxation is a standard concern for in situ stress measurements, being observed on many specimens such as bulk polycrystals[37] or thin films[38] but also in 316L austenitic steel at room temperature.[39] In austenitic steels, it has been reported that the early stages of plastic deformation involve first the activation of lattice dislocations followed by the activation of triple-point sources (absent in our case) and the formation of dislocation pile-ups, with slip transmission across the grain boundaries thereafter.[40] Scanning electron microscopy imaging at high resolution of the grain boundary area showed typical direct slip band transfer across the grain boundary which would support this interpretation and explain why relaxation occurs more specifically near the grain boundary. Recently, a polycrystal mean-field homogenization model coupled with a dislocation-based constitutive relation accounting for statistical distributions of internal stresses was also proposed to reproduce the effect of relaxation (polycrystal average) on neutron diffraction data.[41] This approach was, however, not as concerned with the spatial resolution as that applied here with Laue experiment and full-field finite element modeling. A relaxation effect linked to grain boundaries was not envisioned and it relies on an additional parameter, the standard deviation of the distribution of resolved shear stress. On the experimental side, further investigation of this issue is required, which should now be possible when using the new x-ray detector of BM32 operating at 10 Hz. One could try to monitor the time evolution of elastic strains near a grain boundary, for example. It might also be required to study the slip transfer at the micron scale from the interface, as was carried out in several recent works.[42,43]

Only the results concerning the *yy* component of the stress and strain fields are presented. Laue data were analyzed using the standard method implemented in LaueTools software, in which the position of Laue spots on the x-ray detector screen are compared with theoretical ones computed for an elastically strained Fe crystal lattice. As shown in Refs. 44–46, the DIC technique can be used to estimate very precisely (with accuracy of a few hundredths of a detector pixel) the spot displacement between two loading steps, leading to enhanced accuracy in the stress estimation. On ideal crystals (Si and Ge single crystals), stress accuracy on the order of 1 MPa can be reach by using this Laue–DIC technique. This constitutes another possible continuation of this work, allowing investigation of grain boundary effects on other components of the stress field. This will also make it possible to study lattice rotations with accuracy better than 10^{-4} rad.

The results presented herein suggest that grain boundaries as microstructural objects need special treatment in crystal plasticity modeling, such an accurate definition of subsequent slip transfer,[47] eventually complemented by the effect of incompatibility strains[42,48] and/or strain gradient effects.[49] Applying jump conditions for geometrically necessary dislocations may also be required.[50] Strain rate effects on the slip transfer could also be considered.[51] It may be required to treat the grain boundary as a thin surface with specific properties or special kinematics conditions allowing sliding and torsion.[16] Another class of interface treatment could be to integrate grain boundaries as a nonlocal microstructural constituent with special properties per se.[17] Further progress will require comparison of the results for our geometry using several of these approaches.

CONCLUSION

Attempting to validate elastic strains (e.g., internal stresses) simulated by crystal plasticity with measured ones reveals that they are notably overestimated in the neighborhood of a general grain boundary but reproduced better away from the grain boundary. A refinement of this type of experiment would allow one to exclude artifacts or guide possible extensions of crystal plasticity models (inclusion of relaxation or slip transfer at grain boundaries). One could also explore the extension of such modeling to various, more sophisticated crystal plasticity models, in order to be able to fully reproduce at least the bicrystal case. On the application side, the results of this work demonstrate that the question of internal stresses due to the incompatibility of the deformation at the grain boundary is not yet settled, hindering thorough understanding of intergranular stress-controlled effects that remain a challenge in materials science.

ACKNOWLEDGEMENT

C. Rey is warmly thanked by the authors for many fruitful discussions and for allowing us to use the CristalECP code. The Laboratoire d'Imagerie Biomédical of Sorbonne Université (Paris, France) is acknowledged for its help in measuring elastic constants by ultrasonic means. Beamtime allocation at the French Beamline BM32 CRG-IF at the European Synchrotron Facility (ESRF) is gratefully acknowledged (Award Nos. HC/913 & HC/1449).

REFERENCES

1. D. Dye, H.J. Stone, and R.C. Reed, *Curr. Opin. Solid State Mater. Sci.* 5, 31 (2001).
2. M. Kamaya, Y. Kawamura, and T. Kitamura, *Int. J. Solids Struct.* 44, 3267 (2007).

3. M. Kamaya and M. Itakura, *Eng. Fract. Mech.* 76, 386 (2009).
4. D. Gonzalez, I. Simonovski, P.J. Withers, and J. Quinta da Fonseca, *Int. J. Plastic.* 61, 49 (2014).
5. K. Wierzbanowski, J. Tarasiuk, B. Bacroix, A. Miroux, and O. Castelnau, *Archiv. Metall.* 44, 183 (1999).
6. A. Wauthier-Monnin, T. Chauveau, O. Castelnau, H. Réglé, and B. Bacroix, *Mater. Charact.* 104, 31 (2015).
7. G. Ribárik, J. Gubicza, and T. Ungár, *Mater. Sci. Eng. A* 387–389, 343 (2004).
8. B. Clausen, T. Lorentzen, M.A.M. Bourke, and M.R. Daymond, *Mater. Sci. Eng. A* 259, 17 (1999).
9. J.W.L. Pang, T.M. Holden, J.S. Wright, and T.E. Mason, *Acta Mater.* 48, 1131 (2000).
10. R. Lin Peng, M. Odén, Y.D. Wang, and S. Johansson, *Mater. Sci. Eng. A* 334, 215 (2002).
11. M. Bornert, F. Brémand, P. Doumalin, J.-C. Dupré, M. Fazzini, M. Grédiac, F. Hild, S. Mistou, J. Molimard, J.-J. Orteu, L. Robert, Y. Surrel, P. Vacher, and B. Wattrisse, *Exp. Mech.* 49, 353 (2009).
12. A.J. Wilkinson, G. Meaden, and D.J. Dingley, *Ultramicroscopy* 106, 307 (2006).
13. C. Maurice, J.H. Driver, and R. Fortunier, *Ultramicroscopy* 113, 171 (2012).
14. J.S. Chung and G.E. Ice, *J. Appl. Phys.* 86, 5249 (1999).
15. B. Jakobsen, H.F. Poulsen, U. Lienert, and W. Pantleon, *Acta Mater.* 55, 3421 (2007).
16. V. Taupin, L. Capolungo, C. Fressengeas, M. Upadhyay, and B. Beausir, *Int. J. Solids Struct.* 71, 277 (2015).
17. P.R.M. van Beers, G.J. McShane, V.G. Kouznetsova, and M.G.D. Geers, *J. Mech. Phys. Solids* 61, 2659 (2013).
18. L. Priester, *Grain Boundaries, From Theory to Engineering*, Vol. 172Springer Series in Materials Science, (Berlin: Springer, 2012).
19. C. Teodosiu, J. Raphanel, and L. Tabourot, *Large Plastic Deformations*, ed. C. Teodosiu, J. Raphanel, and F. Sidoro (Rotterdam: A.A. Balkema, 1993), pp. 153–175.
20. L. Méric, P. Poubanne, and G. Cailletaud, *Trans. ASME* 113, 162 (1991).
21. E. Plancher, J. Petit, C. Maurice, V. Favier, L. Saintoyant, D. Loisnard, N. Rupin, J.-B. Marijon, O. Ulrich, M. Bornert, J.-S. Micha, O. Robach, and O. Castelnau, *Exp. Mech.* 56, 483 (2016).
22. E. Plancher, V. Favier, C. Maurice, E. Bosso, N. Rupin, J. Stodolna, D. Loisnard, J.-B. Marijon, J. Petit, J.-S. Micha, O. Robach, and O. Castelnau, *J. Appl. Cryst.* 50, 940 (2017).
23. O. Ulrich, X. Biquard, P. Bleuet, O. Geaymond, P. Gergaud, J.S. Micha, O. Robach, and F. Rieutord, *Rev. Sci. Instrum.* 82, 033908 (2011).
24. O. Robach, C. Kirchlechner, J.S. Micha, O. Ulrich, X. Biquard, O. Geaymond, O. Castelnau, M. Bornert, J. Petit, S. Berveiller, O. Sicardy, J. Villanova, and F. Rieutord, Chapter 5: Laue microdiffraction at ESRF.*Strain and Dislocation Gradients from Diffraction*, ed. R.I. Barabash and G.E. Ice (Singapore: Imperial College Press/World Scientific, 2014), pp. 156–204.
25. J.S. Chung and G.E. Ice, *J. Appl. Phys.* 86, 5249 (1999).
26. E.H. Lee, *J. Appl. Mech.* 36, 1 (1969).
27. P. Franciosi, *Acta Metall.* 33, 1601 (1985).
28. D. Peirce, R.J. Asaro, and A. Needleman, *Acta Metall.* 31, 1951 (1983).
29. P. Erieau and C. Rey, *Int. J. Plast.* 20, 1763 (2004).
30. J. Schwartz, C. Rey, and O. Fandeur, *Int. J. Fatigue* 55, 202 (2013).
31. R.F. Laubscher, Ph.D. thesis, Rand Afrikans University, 1997.
32. B. Devincre, L. Kubin, and T. Hoc, *Science* 320, 1745 (2008).
33. A.J. Beaudouin, M. Obstalecki, R. Storer, W. Tayon, J. Mach, P. Kenesei, and U. Lienert, *Modell. Simul. Mater. Sci. Eng.* 20, 024006 (2012).
34. M.P. Miller and P.R. Dawson, *Curr. Opin. Solid State Mater. Sci.* 18, 286 (2014).
35. C. Rey and A. Zaoui, *Acta Metall.* 28, 687 (1980).
36. C. Rey, *Rev. Phys. Appl.* 23, 491 (1988).
37. R. Dakhlaoui, A. Baczmanski, C. Braham, S. Wronski, K. Wierzbanowski, and E.C. Oliver, *Acta Mater.* 54, 5027 (2006).
38. D. Faurie, P. Djemia, E. Le Bourhis, P.-O. Renault, Y. Roussigné, S.M. Chérif, R. Brenner, O. Castelnau, G. Patriarche, and Ph Goudeau, *Acta Mater.* 58, 4998 (2010).
39. H. Wang, B. Clausen, C.N. Tomé, and P.D. Wu, *Acta Mater.* 61, 1179 (2013).
40. K.J. Kurzydlowski, R.A. Varin, and W. Zielinski, *Acta Metall.* 32, 71 (1984).
41. H. Wang, B. Clausen, L. Capolungo, I.J. Beyerlein, J. Wang, and C.N. Tomé, *Int. J. Plast.* 79, 275 (2016).
42. I. Tiba, T. Richeton, C. Motz, H. Vehoff, and S. Berbenni, *Acta Mater.* 83, 227 (2015).
43. T.R. Bieler, P. Eisenlohra, C. Zhang, H.J. Phukan, and M.A. Crimp, *Curr. Opin. Solid State Mater. Sci.* 18, 212 (2014).
44. J. Petit, O. Castelnau, M. Bornert, F. Zhang, F. Hofmann, A.M. Korsunsky, D. Faurie, C. Le Bourlot, J.S. Micha, O. Robach, and O. Ulrich, *J. Synchr. Rad.* 22, 980 (2015).
45. F.G. Zhang, O. Castelnau, M. Bornert, J. Petit, J.B. Marijon, and E. Plancher, *J. Appl. Cryst.* 48, 1805 (2015).
46. F.G. Zhang, M. Bornert, J. Petit, and O. Castelnau, *J. Synchr. Rad.* 24, 802 (2017).
47. W.A.T. Clark, R.H. Wagoner, Z.Y. Shen, T.C. Lee, I.M. Robertson, and H.K. Birnbaum, *Scr. Metall. Mater.* 26, 203 (1992).
48. J. Gemperlova, V. Paidar, and F. Kroupa, *Czech J. Phys. B* 39, 427 (1989).
49. N.M. Cordero, S. Forest, E.P. Busso, S. Berbenni, and M. Cherkaoui, *Comput. Mater. Sci.* 52, 7 (2012).
50. A. Acharya, *Philos. Mag.* 87, 1349 (2007).
51. N.V. Malyar, G. Dehm, and C. Kirchlechner, *Scr. Mater.* 138, 88 (2017).